Intimate Monolithic Integration of Chip-Scale Photonic Circuits

Vijit A. Sabnis, *Member, IEEE*, Hilmi Volkan Demir, *Member, IEEE*, Onur Fidaner, *Student Member, IEEE*, Jun-Fei Zheng, James S. Harris, Jr., *Fellow, IEEE*, David A. B. Miller, *Fellow, IEEE*, Nelson Li, Ta-Chung Wu, H.-T. Chen, and Yu-Min Houng

Abstract—In this paper, we introduce a robust monolithic integration technique for fabricating photonic integrated circuits comprising optoelectronic devices (e.g., surface-illuminated photodetectors, waveguide quantum-well modulators, etc.) that are made of completely separate epitaxial structures and possibly reside at different locations across the wafer as necessary. Our technique is based on the combination of multiple crystal growth steps, judicious placement of epitaxial etch-stop layers, a carefully designed etch sequence, and self-planarization and passivation steps to compactly integrate optoelectronic devices. This multigrowth integration technique is broadly applicable to most III–V materials and can be exploited to fabricate sophisticated, highly integrated, multifunctional photonic integrated circuits on a single substrate. As a successful demonstration of this technique, we describe integrated photonic switches that consume only a 300×300 μm footprint and incorporate InGaAs photodetector mesas and InGaAsP/InP quantum-well modulator waveguides separated by 50 μm on an InP substrate. These switches perform electrically-reconfigurable optically-controlled wavelength conversion at multi-Gb/s data rates over the entire center telecommunication wavelength band.

Index Terms—Integrated optoelectronic devices, monolithic integration, photonic switches, selective area growth (SAG).

I. INTRODUCTION

CURRENT optical networks require the use of discrete optical and electronic components for performing optical–electronic–optical (OEO) conversion functions such as sending, receiving, regenerating, processing, and routing data. Chip-level integration of electronic and photonic devices on a single substrate increases the reliability, enhances the chip yield, simplifies the design, and reduces the size, power consumption, and cost of OEO conversion. In general, chip-level integration

can be accomplished through either hybrid or monolithic techniques. Hybrid techniques, such as flip-chip bonding, combine multiple devices fabricated on different substrates into a single package. On the other hand, monolithic integration fabricates all devices simultaneously on a single substrate, akin to the manufacturing of silicon integrated circuits. In this case, external interconnection of individual devices is eliminated, and design and testing are performed for the overall integrated system. Furthermore, for high-speed applications, in contrast to hybrid integration, monolithic integration can offer substantial performance advantages by avoiding the use of solder bumps and long metal posts. Since interdevice distances can be minimized and external wire bonding is not required, parasitic resistance, capacitance, and inductance are minimized, providing significant simplifications and improvements in design flexibility and ultimate circuit performance.

Currently, only group III–V material systems, such as GaAs and InP, along with their compatible ternary or quaternary alloys, can be used to fabricate high-speed, high-performance electronic and photonic devices suitable for data processing. Complex monolithic integration of different group III–V devices on a single substrate, however, is a relatively immature technology. Most researchers have focused on monolithic integration techniques that allow fabricating multiple optical devices along a single or set of optical waveguide(s) [1]–[3], for example, diode lasers integrated with electroabsorption modulators and semiconductor optical amplifiers. In these demonstrations, the integrated devices have similar device and epitaxial structures with the exception of the inclusion or exclusion of a thin active layer located in the core of the shared waveguide. Other researchers have investigated integrating p-i-n photodiodes with electronic amplification and signal processing circuitry in which a single set of epitaxial layers is grown and then processed [4].

In this work, we developed and demonstrated a monolithic process for on-chip intimate integration of a waveguide electroabsorption modulator (EAM) and a surface-illuminated *p-i-n* diode mesa photodetector (PD), both of which consist of completely different epitaxial layers except for the starting layers, along with other components to make a high-speed optically-controlled optical switch [5], [6]. We report a multigrowth monolithic integration technique [7] that incorporates a special etch sequence and self-planarization and passivation [8], [9] steps to enable chip-scale photonic circuit integration. To the best of our knowledge, few other groups have recently attempted to integrate surface-illuminated and waveguide-coupled optoelectronic devices monolithically on a single chip [10]–[13].
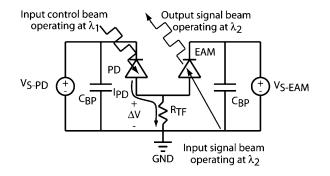
Fig. 1. Circuit diagram and principle of operation of PD-EAM photonic integrated circuit [6].

This integration technique forms the basis for application to other complex multifunctional photonic integrated circuits.

In Section II, we outline the device concept briefly and the integration requirements in detail. (More information on the device operation and testing can be found in [5], [6], [14]). In Section III, we describe and illustrate our monolithic integration process, comprising a two-step epitaxial growth sequence, the etch techniques used to define the PD mesas and EAM waveguides, device planarization and passivation, thin film resistor deposition, and metal interconnection. For validation of this integration technique, in Section IV we present proof-of-concept experimental results of high-speed optical switching and wavelength conversion from our devices before concluding in Section V.

II. PHOTODIODE-MODULATOR PHOTONIC INTEGRATED CIRCUITS

A. Integrated PD-EAM Switch Concept

Fig. 1 shows the circuit diagram of a PD-EAM photonic integrated circuit [6]. This circuit, in effect, performs ultra-compact OEO conversion without the use of traditional receiver and transmitter electronic circuitry. The surface-normal input control data stream operating at a wavelength λ_1 is incident on the photodetector. In the presence of the control data stream (i.e., an optical 1 bit), the PD generates a photocurrent I_{PD} that reduces the net reverse bias across the EAM. Consequently, the optical transmission of a continuous-wave signal beam at a wavelength λ_2 that is edge-coupled into the waveguide EAM increases and the corresponding optical 1 bit is observed at the output. In the absence of the control data stream on the PD (i.e., an optical 0 bit), the optical transmission of λ_2 through the EAM remains low, resulting in a corresponding optical 0 bit at the output. The modulation in the EAM is achieved through the quantum confined Stark effect [15].

For switch operation, the PD is reverse-biased to ensure high-speed photocurrent extraction, while the EAM is reverse-biased such that quantum wells located in the core of the waveguide strongly absorb at λ_2. The switching bandwidth, neglecting parasitics, is controlled by the *RC* time constant of the internal circuit and is given by (1) [6]:

$$f_{3\,\text{dBe}} = \frac{\sqrt{3}}{2\pi R_{TF}(C_{PD} + C_{EAM})}. \tag{1}$$

Both the PD and the EAM are fabricated from p-i-n diode structures and are independently reverse-biased through a pair of voltage supplies, $V_{S\text{-}PD}$ and $V_{S\text{-}EAM}$, respectively. Biasing for both devices is provided across two large bypass capacitors (C_{BP}), ~ 500 pF, to ensure that the high-speed electronic switching is localized to the integrated circuitry between both capacitors. The PD and EAM circuits are coupled through a thin-film resistor (R_{TF}), which is connected between the shared p-contact of the PD-EAM and ground (GND).

The PD-EAM photonic integrated circuit provides optical switching, wavelength conversion, multi-wavelength broadcasting, partial optical regeneration, space switching, and packet switching, all possibly provided at the same time for multiple channels on a single integrated chip [5], [6], [14], [16], [17]. It features multi-gigabit per second switching operation over the entire center telecommunication wavelength band (C-band) while requiring only milliwatt-level optical/electrical switching powers. Furthermore, our integration technique enables compact circuit integration into an area of only 300×300 μm. A single packaged chip of the PD-EAM photonic integrated circuit could displace, in certain optical networking applications, multiple discretely-packaged and interconnected electronic and optical components found in traditional OEO conversion modules.

B. PD-EAM Switch Circuit-Integration Requirements

The integration requirements of our PD-EAM photonic integrated circuit are typical in that the implementation of any integrated, high-speed photonic circuit requires compact integration and low parasitics. For the PD-EAM switch, a monolithic process must intimately fabricate the entire circuit in a size scale much smaller than the wavelength of any of the electrical frequencies involved, enabling the switch to operate as a lumped circuit and precluding the need for incorporating transmission lines or other microwave circuitry inside the device. Electrical parasitics that unnecessarily degrade the device switching bandwidth and increase the required optical switching power are also minimized by such an intimate integration process. Moreover, the integration technique must incorporate PD and EAM structures comprising separately optimizable epitaxial layers for better performance, including bi-directional wavelength conversion. This also eliminates other problems associated with a single diode implementation of such a switch [18]. Finally, the integration technique must also conveniently enable fabricating two-dimensional arrays of devices and possess scalability for high-speed switching operation.

Hybrid integration techniques can be used to construct the PD-EAM photonic integrated circuit and are attractive because they allow each circuit component to be individually designed and processed prior to integration, reducing the overall fabrication tolerances and risks. The simplest hybrid integration approaches are to wire bond or flip chip bond a separately fabricated PD chip, EAM chip, and resistor chip together into the circuit shown in Fig. 1. Such techniques are relatively easy to implement, though they should be considered only as preliminary solutions due to the problems associated with them. Wire

bonding increases the overall circuit size and both techniques introduce unwanted capacitance and inductance, thereby increasing the required optical switching power and potentially introducing design complexity through the introduction of unnecessary electrical impedance in the circuit. Indeed, unless the wire bond is very short, such a wire bonded switch will not work due to the added capacitance of the wire. Although these concerns may not be problematic for switch operation up to a few Gb/s, they will substantially deteriorate the switching performance at speeds of 10 Gb/s and beyond. Furthermore, wire bonding is not practically feasible for constructing large two-dimensional (2-D) matrices of PD-EAM photonic integrated circuits.

Monolithic integration techniques can also be used to fabricate the PD-EAM photonic integrated circuit without compromising scalability for high-speed and 2-D array operation. The most straightforward monolithic integration technique requires growing the EAM and PD epitaxy on top of each other in a single growth step, creating, for example, a *p-i-n-p-i-n* or *n-i-p-i-n* diode stack. This method introduces a multilevel mesa structure and creates several challenges for lithography, where depth-of-focus limitations may create difficulties in patterning the various circuit components, and electrical interconnection, where multilevel routing of electrical interconnect metal would be required. Furthermore, such an approach introduces parasitics, again degrading the speed performance of the integrated device, through the introduction of capacitance from unused diode epitaxy that is unnecessarily incorporated into the circuit. To avoid these problems, we developed a monolithic integration technique that we discuss in the next section. The technique employs selective area growth (SAG) [19]–[22] based on metal-organic chemical-vapor deposition (MOCVD) [23]. This approach enables approximately planar, side-by-side integration of separate PD and EAM structures, without compromising individual component design.

III. MONOLITHIC INTEGRATION PROCESS

A. PD-EAM Integration Overview

There are five main features of our integration process: a) the incorporation of buried epitaxial etch stops for proper SAG surface preparation and device isolation; b) a selective area growth process that enables compact integration of different epitaxial structures; c) an SAG epitaxy etch technique employing selective wet etches and shallow dry etches for creating device mesas in the SAG area; d) a polymer planarization and passivation process that ensures device reliability and enables electrical interconnection of different devices; and e) a planarization-polymer etch process that allows multilevel metal routing as required by the circuit architecture. As an example of these integration techniques, in the following sections, we discuss how the above techniques are used to enable robust monolithic integration of PD-EAM photonic integrated circuits.

Tables I and II show the EAM and PD epitaxial layer structures, respectively. A detailed discussion of the epitaxial layer design can be found in [6]. The EAM is a *p-i-n*-diode waveguide structure containing ten strained-InGaAsP quantum wells

TABLE I
EAM EPITAXIAL LAYER STRUCTURE

	Material and Thickness		Doping (cm^{-3})
19	500 Å InGaAs		*p*-Zn, 1x10^{19}
18	10000 Å InP		*p*-Zn, 5x10^{17}
17	3000 Å InP		*p*-Zn, 1-5x10^{17}
16	1950 Å InP		u.i.d
15	200 Å 1.1Q In$_x$Ga$_{1-x}$As$_y$P$_{1-y}$		u.i.d
14	200 Å 1.2Q In$_x$Ga$_{1-x}$As$_y$P$_{1-y}$		u.i.d
13	200 Å 1.3Q In$_x$Ga$_{1-x}$As$_y$P$_{1-y}$		u.i.d
12	60 Å 1.22Q In$_x$Ga$_{1-x}$As$_y$P$_{1-y}$	(x 10)	u.i.d
11	80 Å 1.56Q In$_x$Ga$_{1-x}$As$_y$P$_{1-y}$		u.i.d
10	60 Å 1.22Q In$_x$Ga$_{1-x}$As$_y$P$_{1-y}$		u.i.d
9	200 Å 1.3Q In$_x$Ga$_{1-x}$As$_y$P$_{1-y}$		u.i.d
8	200 Å 1.2Q In$_x$Ga$_{1-x}$As$_y$P$_{1-y}$		u.i.d
7	200 Å 1.1Q In$_x$Ga$_{1-x}$As$_y$P$_{1-y}$		u.i.d
6	390 Å InP		u.i.d
5	8500 Å InP		*n*-Si, 5x10^{17}
4	200 Å 1.3Q In$_x$Ga$_{1-x}$As$_y$P$_{1-y}$		*n*-Si, 3x10^{18}
3	5500 Å InP		*n*-Si, 5x10^{17}
2	200 Å 1.3Q In$_x$Ga$_{1-x}$As$_y$P$_{1-y}$		u.i.d
1	2500 Å InP		u.i.d
0	(substrate) semi-insulating InP		Fe

u.i.d: unintentionally doped

TABLE II
PD EPITAXIAL LAYER STRUCTURE

	Material and Thickness		Doping (cm^{-3})
13	500 Å InGaAs		*p*-Zn, 1x10^{19}
12	1000 Å InP		*p*-Zn, 3x10^{18}
11	2300 Å InP		*p*-Zn, 5x10^{17}
10	3000 Å InP		*p*-Zn, 1-5x10^{17}
9	1500 Å InP		u.i.d
8	200 Å 1.1Q In$_x$Ga$_{1-x}$As$_y$P$_{1-y}$		u.i.d
7	200 Å 1.2Q In$_x$Ga$_{1-x}$As$_y$P$_{1-y}$		u.i.d
6	200 Å 1.3Q In$_x$Ga$_{1-x}$As$_y$P$_{1-y}$		u.i.d
5	12500 Å InGaAs		u.i.d
4	3300 Å InP		*n*-Si, 3x10^{17}
3	5500 Å InP (Si, 5.0x10^{17})		*n*-Si, 5x10^{17}
2	200 Å 1.3Q In$_x$Ga$_{1-x}$As$_y$P$_{1-y}$	EAM layers	u.i.d
1	2500 Å InP		u.i.d
0	(substrate) semi-insulating InP		Fe

u.i.d: unintentionally doped

designed to provide efficient electroabsorption over the C-band. The PD epitaxy starts on top of layer 3 of the EAM epitaxy and comprises a *p-i-n*-diode surface-illuminated photodetector structure with an InGaAs intrinsic layer that provides broadband photoabsorption for wavelengths smaller than 1650 nm.

Fig. 2 shows a summary of the first several steps of the PD-EAM photonic integrated circuit process. Instead of consecutively growing the EAM and PD epitaxial layers in a single step, an epitaxial regrowth step is used to incorporate the PD layers after growth and modest processing of the EAM layers. After growing the EAM epitaxial layers on a semi-insulating InP wafer [see Fig. 2(a)], the wafer is dry-etched to create a periodic array of EAM ridge waveguides [see Fig. 2(b)] and encapsulated in a dielectric material [see Fig. 2(c)]. The PD epitaxy layers
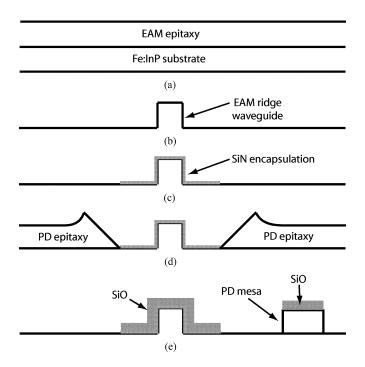
Fig. 2. Selective area growth process for integrating PD and EAM: (a) EAM epitaxial growth, (b) EAM ridge etch, (c) SAG SiN nitride mask definition, (d) PD SAG, and (e) PD mesa etch. Not drawn to scale.
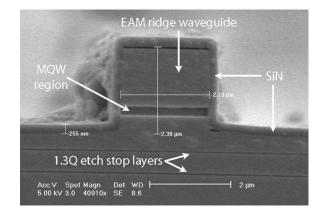

Fig. 3. Scanning electron microscope (SEM) picture of stain-etched EAM waveguide area. The two dark lines running horizontally within the lower waveguide cladding are each 200-Å-thick 1.3Q etch-stop layers.

are then deposited using an SAG process employing MOCVD [see Fig. 2(d)]. The PD mesas are subsequently etched in the area adjacent to the EAM [see Fig. 2(e)], resulting in intimate integration of both components. The advantage of this implementation is that the overall final structure can be designed to be approximately planar and, hence, it is significantly more straightforward to process than a single-step epitaxially grown structure. Subsequent steps complete the device integration by providing dielectric (e.g., polymer) planarization-passivation of the devices, thin film resistor deposition, and appropriate metal interconnection and routing.

B. Buried Etch-Stop Layers for SAG Surface Preparation

A key feature of the PD and EAM structures is the use of buried etch stop layers. These etch stop layers enable robust integration of different epitaxial layers by providing the ability to achieve clean, planar surfaces prior to epitaxial regrowths or after mesa/ridge etching. For the PD-EAM photonic integrated circuit a 200-Å-thick 1.3Q etch-stop layer (Table I layer #4) is located part way into the bottom n-doped EAM cladding and a second etch-stop layer (Table I layer #2), shared with the PD, is located underneath the bottom waveguide cladding. Fig. 3 shows a stain-etched cross section of the EAM ridge waveguide area, clearly showing the buried etch-stop layers.

After the growth of the EAM epitaxial layers, the wafers are masked with SiN and patterned into stripes. The EAM ridge waveguides are then created using an inductively-coupled reactive-ion etch using Cl_2 and HBr gases. The etch depth is chosen so that the ridge height falls into the upper part of the n-doped InP cladding layer (Table I layer #5), but above the

1.3Q etch-stop layer (Table I layer #4). The ridge waveguides and 5–10 μm of surrounding area are subsequently masked off with another SiN layer to prepare for SAG. A selective InP wet etch (1 HCl: 3 H_3PO_4) is used to remove the remaining InP in layer #5, stopping on the 1.3Q etch-stop layer. The etch-stop layer ensures a clean surface with approximately perfect uniformity over the entire wafer surface, which is critical for achieving reproducible SAG results. Finally, a selective 1.3Q etch (1 H_2SO_4:8 H_2O_2:40 H_2O) is used to remove the etch-stop layer, exposing a clean InP layer over the entire wafer and allowing the wafer to be regrown on using SAG.

This technique can be generalized for devices requiring multiple SAG steps. For devices sharing a common bottom-doped epitaxial layer, multiple etch-stop layers—one for each SAG step—can be buried within the common doped layer to enable sequential surface preparation for SAG. For devices requiring different doping types or levels for their bottom layers, these different doped layers need to be grown sequentially in the first epitaxial growth step with a buried etch-stop layer located in each appropriate layer. Furthermore, this technique should also be applicable to the GaAs–AlGaAs-based material system. In this case, InGaP lattice matched to GaAs can serve as a selective etch-stop layer since it is not attacked by most wet etch chemistries used to remove GaAs–AlGaAs materials.

C. Selective Area Growth Integration

We performed a series of studies to understand the characteristics and capabilities of SAG and to achieve a robust and reproducible SAG process. The MOCVD growths were performed using a Thomas Swan close-coupled showerhead reactor employing trimethylindium (TMIn) gas as the In source, trimethylgallium (TMGa) as the Ga source, 100 ppm Si_2H_6/H_2 as the Si source, diethylzinc (DZ) as the Zn source, AsH_3 as the As source, PH_3 as the P source, and H_2 as the carrier gas. The epitaxy was grown at $650°$ C at a growth pressure of 100 torr. The carrier gas flow was $\sim$20 lpm, the V–III flow rate ratio was $\sim$100, and the substrate rotation during growth was 100 rpm.

Fig. 4 shows a SEM picture of a portion of a regrown wafer. The thin stripe crossing through the center of the picture is the
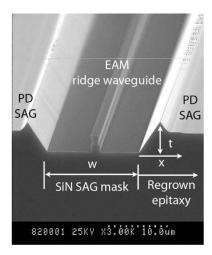
Fig. 4. SEM picture showing PD SAG epitaxy adjacent to SiN-masked EAM ridge waveguide area.
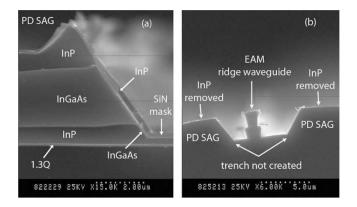

Fig. 5. (a) SEM picture of stain-etched PD SAG epitaxy where each epitaxial layer encapsulates lower layers and (b) PD SAG epitaxy after removal of upper InP layer using a selective wet etch. The etch does not create a trench at the interface between the SAG and masked-EAM areas, confirming encapsulation of SAG layers.

EAM ridge waveguide, which runs continuously from one end of a two inch wafer to the other end. A $w = 15$ μm wide SiN mask encapsulates the waveguide, and this masked area repeats laterally every 500 μm across the entire width of the wafer. The areas outside the SiN masked area contain selectively grown PD epitaxy.

By examining such wafers, we find that there are three main characteristics of SAG that are necessary to consider for compactly integrating the PD and EAM. The composition of the material grown near the SAG mask edge is different than it is at locations far from the mask edge. For InGaAs and InGaAsP growths, epitaxy near the mask edge incorporates a larger In mole fraction, resulting in compressive strain and large shifts in bandgap energy. This compositional variation gradually tapers off with increasing distance from the mask edge. This characteristic can be advantageous for integrating active and passive waveguide devices on chip, but in our case we need to avoid this region to ensure reliable and high-performance PD operation. The enhanced In incorporation can be explained by the lower decomposition temperature of TMIn gas compared with TMGa gas, resulting in a higher concentration and effective diffusion coefficient of In species. Since deposition does not occur on the SAG mask, there is a larger proportion of In species near the mask edge than further away. An alternative explanation [19] suggests that it is easier to break a methyl–indium bond compared to a methyl–gallium bond at the substrate surface, allowing for the increased incorporation of In compared to Ga near the mask edge.

The second major characteristic of SAG is that each epitaxial layer completely encapsulates all underlying SAG layers. This is particularly important at the interface between the SAG area and the masked area; the encapsulation can be seen very clearly in Fig. 5(a), which shows a SEM cross-sectional picture of stain-etched PD SAG epitaxy adjacent to the SiN-masked EAM waveguide area. In this figure the upper InP layer seals the InGaAs absorber layer at locations far from the mask edge where the SAG epitaxy shape is stable and continues to do so all the way to the interface with the SiN mask where the SAG epitaxy exhibits a sloped shape. Similarly, the InGaAs absorber seals the

lower InP n-doped layer. Fig. 5(b) confirms the epitaxial-layer encapsulation by showing the PD SAG area after the sample has been dipped in a selective InP etch. The upper InP layer of the PD epitaxy has been removed without damage to the underlying layers. In particular, a trench has not been created at the SiN mask edge, which would preclude convenient routing and interconnection of the EAM n-metallization. In this case, the trench can not be created since the InGaAs layer grown prior to the upper InP layer is present at the interface with the SiN mask.

As can be seen in Figs. 4 and 5, the third major characteristic of SAG is an increased growth rate near the SAG mask edge. This enhancement is caused by lateral vapor phase diffusion above the SAG mask that supplies additional reactants to the unmasked area. The SAG growth rate is a strong function of the width of the SAG mask and the width of the unmasked area. As the SAG mask width increases, the growth rate near the mask edge increases due to the increase in lateral supply of reactants coming from the masked area. Similarly, as the width of the unmasked region decreases, the SAG growth rate near the mask edge also increases since the lateral supply of reactants from the masked area is consumed over the smaller unmasked area. There is a strong crystallographic dependence on the shape of the regrown epitaxy. In Fig. 4, the EAM waveguides are oriented in the (011) direction. The sloped area near the SAG mask edge corresponds to the (111)B crystal plane. Epitaxy grows slower on this plane than on the (001) plane because the dangling bond density of the (111)B plane is approximately 42% lower than on the (001) plane [19]. During growth, Group III reactants migrate from the lower bonding density (111)B plane to the higher bonding density (001) plane, creating the spiked-shape feature near the mask edge.

We designed our integration process to incorporate the PD epitaxy after the growth of the EAM epitaxy, rather than the opposite order, to avoid complications arising from the thickness and composition characteristics of SAG. The EAM epitaxy contains strained-InGaAsP quantum wells with an absorption band edge located approximately at 1480–1490 nm. Integrating
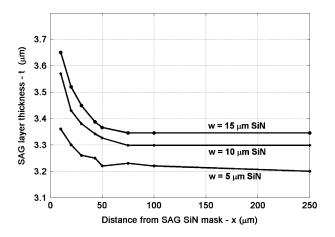
Fig. 6. Thickness of SAG epitaxy (t) versus distance from SiN SAG mask (x) for three SAG masks widths (w).

the EAM using SAG may produce thicker quantum wells with a larger In content, resulting in a displaced absorption band edge and reduced electroabsorption performance. Although these effects could be eliminated or compensated through an extensive set of SAG studies, it is easier and less risky to perform SAG of the PD epitaxy. Furthermore, the PD photodetection characteristics are not extremely sensitive to the exact thickness of the absorbing intrinsic region, which is made up of InGaAs lattice-matched to InP. The main requirement is that the PD needs to be fabricated far enough away from the mask edge to ensure that the InGaAs is not highly strained, ensuring reliable PD operation with strong absorption over the C-band.

In order to determine the minimum distance that the PD and EAM can be fabricated from each other, we measured the thickness, t, of the SAG epitaxy as a function of distance from the mask edge, x, for 5, 10, and 15 μm SiN SAG mask widths, w, using scanning electron microscopy (see Fig. 4). Although this measurement does not provide information about the strain present in the SAG epitaxy, for this particular geometry, it is a reasonable assumption that the epitaxial compositional variation approximately follows the SAG thickness variation. Fig. 6 shows a plot of the SAG epitaxial thickness t versus x for 5-, 10-, and 15-μm SAG mask widths. As expected, as the mask width increases, the SAG thickness enhancement increases. For all three mask widths, the SAG thickness stabilizes after approximately 50 μm, although the stabilized thickness is different for each mask width, indicating an overall thickness enhancement compared to growth on an unmasked substrate. From these results, we can conservatively estimate a minimum required separation of 50 μm between the PD and EAM. This is a relatively small spacing, and the necessary 50-μm-long electrical interconnect between the PD and EAM will not introduce any significant electrical parasitics. If we consider 50 μm to be the minimum size-scale limit for integration of the various circuit components, lumped-circuit operation of such integrated optoelectronic circuits up to 40 Gb/s should be achievable since the electrical wavelength at these speeds is approximately 2 mm, which is more than 10 times larger than the minimum device separation. Hence, this selective area growth technique provides for com-

pact integration of the optoelectronic components that should easily accommodate high-speed operation.

For the PD-EAM switch integration we designed the thickness of the PD epitaxy to be approximately 2500 Å thinner than the EAM epitaxy to compensate for the thickness enhancement provided by SAG. This allows the uppermost surfaces of the PD and EAM to be approximately planar after SAG, making subsequent polymer planarization and electrical interconnection convenient. Note that in general, epitaxial structures from different growth steps can be designed so that they are approximately planar with each other through the incorporation of dummy or sacrificial layers (i.e., doped or undoped InP–GaAs, depending on the material system used).

D. SAG Epitaxy Patterning

In many cases, SAG will result in modified growth features near the SAG mask edge, as shown in Figs. 4 and 5, which can be problematic for device integration. Although fabricating mesa structures in the SAG area does not present any unique challenges by itself, it is often times desirable or necessary to create these mesas while simultaneously creating a planar interface between the SAG area and the masked area to allow for convenient interconnection of devices residing in these different growth areas. The modified growth features near the mask edge often complicate this requirement since a simple nonselective mesa etch in the SAG area will not produce the desired interface; for example in the case of Fig. 5(b) a trench would be created at the interface. The encapsulation of the SAG epitaxy, as discussed in the previous section, is critical because it enables one to use a series of selective wet etches [24] and shallow dry etches to fabricate mesas in the SAG area, while creating an approximately smooth, planar surface at the SAG interface. The selective wet etches allow the SAG epitaxial layers to be removed sequentially, while the shallow dry etches are used only to remove layers that are difficult to wet etch selectively.

For the PD-EAM switch, once the PD SAG is completed, SiO_2 is deposited and patterned as a mask for the PD mesas. We etch the PD mesas [see Fig. 2(d)] using a five-step sequence of dry and wet etches. A selective InGaAs etch (1 H_2SO_4:8 H_2O_2:40 H_2O) removes the top InGaAs p-contact layer (Table II layer #12), followed by a selective InP etch (1 HCl: 3 H_3PO_4) that etches down to the graded quaternary layers (Table II layer #8). Next, a short reactive ion etch using a methane-hydrogen-argon gas chemistry [25] removes the graded quaternary layers (Table II layers #6–8), stopping a few hundred angstroms inside the InGaAs absorber region. A long selective InGaAs(P) etch (1 H_2SO_4:8 H_2O_2:40 H_2O) removes the InGaAs absorber region (Table II layer #5). During SAG, the interface between the bottom n-doped InP layer and the InGaAs absorber is not abrupt, resulting in a parasitic InGaAsP interfacial layer. The degree of phosphorous incorporation is more severe near the SAG mask edge than further away, resulting in an InGaAsP layer whose thickness tapers off with increasing distance from the mask edge. In order to remove this layer, we significantly overetch on this step, creating a lateral undercut of the InGaAs
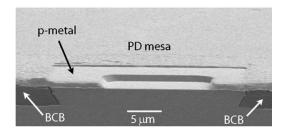
Fig. 7. SEM picture of PD mesa after mesa etching, planarization, and p-metal deposition.

absorber region within the PD mesa. This undercut, however, is advantageous because it ensures complete encapsulation of the intrinsic region by the planarization/passivation material (bisbenzocyclobutene—BCB) that is applied and etched back in a later processing step. The undercut additionally reduces the PD capacitance, improving switching performance [8]. Finally, a second shallow reactive ion etch removes any remaining parasitic InGaAsP and continues approximately 1000 Å within the underlying n-doped InP layer (Table II layer #4). Fig. 7 shows a cross-sectional SEM picture of a finished PD structure. Most importantly, this process creates a smooth interface between the PD SAG area and the EAM area since primarily selective wet etches are used to create the PD mesas. This technique can be generally applied to devices where the mesa sidewall profile created by selective wet etches is not deleterious. If perfectly straight sidewalls are required, then it is likely that an alternate etching technique must be used.

E. Buried Etch-Stop Layers for Device Isolation

A second use for the buried etch-stop layers is to assist in providing device isolation. Once the various mesas in the different regions of the wafers have been created, it is typically necessary to electrically isolate the individual devices. By burying an etch-stop layer below all the doped device layers, one can easily use selective wet etching to create electrical-isolation mesas around the individual devices which extend into a nominally undoped layer or semi-insulating substrate.

For the PD-EAM switch integration, after the PD mesa definition, the surrounding areas of the PD and EAM are masked off with photoresist to define the n-regions of both devices. We employ a three-step wet etch sequence to isolate the PD and EAM devices from each other. First, a selective InP etch (1 HCl: 3 H_3PO_4) removes the exposed n-doped InP material (Table II layer #4-#3), stopping on the bottom etch-stop layer (Table II layer #2). The presence of the bottom etch-stop layer ensures that a planar, uniform etch depth is achieved over the entire sample area, despite the different starting thicknesses of the n- doped InP in the PD and EAM areas. Second, a selective InGaAsP etch (1 H_2SO_4:8 H_2O_2:40 H_2O) removes the bottom etch-stop layer, and finally a subsequent selective InP etch (1 HCl: 1 H_2O) removes the unintentionally doped InP buffer layer (Table II layer #1) and continues a few thousand angstroms within the semi-insulating InP substrate, providing device isolation.

F. BCB Planarization and Passivation

The use of device mesas produces two challenges for complex chip-scale monolithic integration: passivation and planarization. On an InP platform, many electronic and optoelectronic devices are deleteriously affected by conductive native oxides that form on mesa sidewalls and consequently increase device leakage currents, reduce breakdown voltages, and decrease device reliability and lifetime. Passivation of mesa sidewalls with a dielectric material such as SiN or bisbenzocyclobutene (BCB) can alleviate this problem by preventing or reducing oxide formation. Complex circuit architectures may also require electrical interconnection between multiple devices that reside at different heights due to the mesa architecture of the devices of interest. In the silicon integrated circuit industry dielectric deposition, chemical-mechanical polishing, via etching, plug metallization, and metal interconnection are mature processes. However, a comparable set of technologies for compound semiconductors does not exist.

Passivation and planarization are critical issues for the PD-EAM switch integration. It is well known that parasitic In_xO_y forms on the sidewalls of InP-based devices that can significantly degrade device performance. The oxide formation is particularly severe when the device operation temperature exceeds 40–50° C. The PD-EAM switch also requires planarization since electrical interconnection of the PD and EAM p-regions which reside on the uppermost surfaces of each device is required. This metal line needs to be further routed to make contact to the on-chip integrated resistor, which is at the substrate level.

In order to satisfy these requirements, we developed a self-planarization-passivation process using a low-κ dielectric material called BCB [8]. We spin on and cure a $\sim$10-μm-thick BCB film, creating a glass-like material over the wafer surface. The etch-back process, used to planarize the BCB film with the top of the device mesas, is performed using a UHF plasma etcher in two steps. In the steps leading to this etch-back step, the top of the PD mesa was masked with SiO and the EAM waveguides were encapsulated in SiN [see Fig. 8(a)]. The first step in the etch-back process utilizes a specifically designed recipe that offers large selectivity between BCB and SiN/SiO. This etch recipe is used to remove the BCB until the first exposure of the top of the SiN-encapsulated EAM ridge waveguides. The second step utilizes a different recipe that possesses only slight selectivity between BCB and SiN/SiO. This step removes BCB and SiN from the top surfaces of the waveguides, creating a clean surface for p-metallization of the EAMs. For the EAM, both BCB and the encapsulating SiN layer serve as sidewall passivation materials, while for the PD, only BCB is used. During this step, we focused our attention on properly clearing the BCB-SiN from the EAM waveguides only. Once this step is completed, however, the PD is automatically quasi-planarized with the EAM since we deposited a thick oxide film on top of the mesa area prior to the PD mesa definition step. This oxide film is subsequently removed allowing access to the p-region of the PD. Fig. 7 shows a cross section of a planarized PD, while Fig. 9(a) shows a similar cross section of a planarized
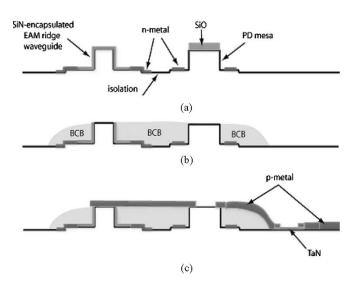
Fig. 8. Illustration of photonic switch cross section after (a) n-contact deposition, (b) BCB planarization, passivation, and patterning, and (c) TaN and p-metal deposition. Note: The features in this illustration are not drawn to scale.
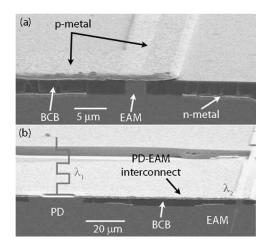

Fig. 9. SEM cross sections of (a) the planarized EAM ridge waveguide and (b) planarized PD-EAM integrated switch.

EAM. Fig. 9(b) is a demagnified cross-sectional picture showing the planarized PD and EAM from one integrated switch along with the interconnecting p-metallization that is deposited in a later step. This technique can be used to planarize and passivate a wide variety of semiconductor structures. An extended discussion of this technique can be found in [8].

G. BCB Patterning for Multilevel Interconnect Routing

Once wafer planarization has been achieved, there still exists the additional challenge of routing interconnect metal from one level to another. This could be achieved using vias and plug metallization, however, these techniques are not mature in compound semiconductor processing technology. An alternative solution is to etch the planarization material such that a slope is created at the interface between two levels where metal interconnection is required. In this way, metal can simply be deposited where needed and travel from one level to another level as required by the circuit architecture.
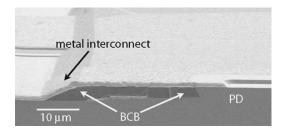

Fig. 10. SEM cross section showing tapered BCB profile enabling metal interconnect to run from top p-contact of PD and EAM to the substrate level.
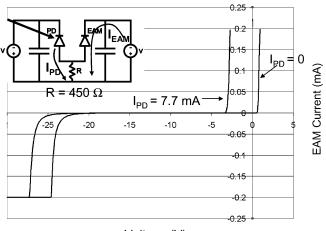
For the PD-EAM switch integration, in order to have access to the n-contact layers of the PD and EAM, to create approximately planar probe contact pads, to provide space for the TaN on-chip resistor, and to clear lines for waveguide cleaving, the BCB must be selectively removed in many places across the sample. We use an SF_6/O_2-based reactive ion etch (RIE) process that attacks BCB and photoresist with little selectivity. After the lithography is completed, the photoresist is reflown to provide a tapered thickness near the edges of the photoresist pattern. We perform the RIE step until the substrate is clear of BCB in the unmasked areas. The BCB underneath the tapered photoresist boundaries also acquires this tapered shape since there is little etch selectivity between the two materials. This creates a sloped BCB region between the top of the BCB and the substrate, conveniently allowing smooth multilevel routing of the p-metalization from the top of the BCB (PD and EAM p-contact level) to the substrate [see Fig. 8(b)]. Fig. 10 shows a picture of the tapered BCB profile created by the above technique.

H. Other Steps

The other steps in the PD-EAM integration process include standard electron-beam evaporation of p- and n-metals, sputtering of TaN [26] for thin film resistor deposition [see Fig. 8(c)], and contact annealing for the formation of ohmic contacts. The wafers are then lapped to a thickness of 120 μm, cleaved into 200–300-μm-long bars (along the direction of the EAM waveguides), and mounted into a copper fixture.

IV. INTEGRATION VALIDATION: PROOF-OF-CONCEPT DEMONSTRATION

As a successful demonstration of the integration techniques described in the previous section, Fig. 11 demonstrates the fundamental optoelectronic functionality of the PD-EAM switch shown in Fig. 1. Here we show the EAM current, I_{EAM} versus the EAM supply voltage, $V_{\text{S-EAM}}$ in the absence and in the presence of a continuous-wave beam incident on the PD. By examining the circuit configuration shown in Fig. 1, we find that current from the PD results in a voltage drop across the on-chip integrated TaN resistor. Consequently, the voltage at the p-side of the EAM increases in the presence of photocurrent from the PD, thereby reducing the voltage drop across the EAM. When sweeping the EAM supply voltage in the presence of photocurrent from the PD, a larger reverse bias across the EAM is needed to achieve the same current level than in the absence of

Fig. 11. EAM current as a function of supply voltage for $I_{\mathrm{PD}} = 0$ and 5 mA. The shift is 3.6 V.
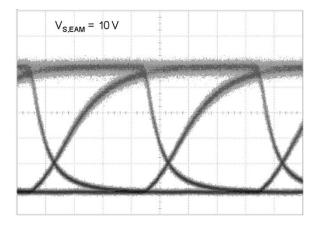

Fig. 12. 1.25 Gb/s eye diagram of PD-EAM integrated photonic switch operation. The data stream incident on the PD has an average power of 5.6 mW at 1552 nm, while the EAM output (shown above) operates at 1556 nm and exhibits greater than 10 dB RF extinction ratio. The PD supply voltage is 15 V, while the EAM supply voltage is 10 V.

photocurrent from the PD. Hence, light shining on the PD, which in turn generates a PD photocurrent, controls the voltage across the EAM. In Fig. 11, we find that in the presence of 7.7 mA of PD current the EAM IV curve is shifted by 3.6 V towards larger reverse biases. This voltage shift is in good agreement with the approximate expected shift of 7.7 mA $\times$ 450 Ω, where 450 Ω is the resistance value of the on-chip resistor.

Fig. 12 demonstrates dynamic operation of the PD-EAM integrated photonic switch. In particular, this result shows wavelength conversion from 1552 nm (incident on the PD) to 1556 nm (exiting the EAM) at 1.25 Gb/s. In this case, the PD supply voltage was 15 V, the EAM supply voltage was 10 V, and the average optical power for the PD was 5.6 mW. The data stream exiting the EAM exhibited an RF extinction ratio greater than 10 dB. The device shown in Fig. 12 was intentionally designed to operate at this relatively low switching speed for proof-of-concept purposes and was not limited by any fundamental parasitics introduced by the fabrication techniques discussed in this paper. In general, for any PD and EAM wavelengths within the

C-band this switch is capable of high-performance wavelength conversion, data broadcasting, partial optical regeneration, and space switching when operating within a 2-D array of switches. Detailed discussions of the device design and functionality, as well as demonstrations of high-speed operation, can be found elsewhere [5]–[9], [14], [16]–[18].

V. Conclusion

In conclusion, we report in this paper a monolithic integration technique that can be utilized to intimately integrate multiple optoelectronic devices in different geometries (waveguide and mesa) with largely different epitaxial layers, all on a single chip. This approach allows for the realization of compact, high-speed integrated photonic circuits on III–V platforms. The important features of this integration method include: 1) the use of multiple selective area regrowths (where completely different epitaxial layers can be grown), 2) the use of selective etch-stop layers (for providing reliable SAG integration and device electrical isolation), 3) the use of a carefully designed sequence of dry and wet etches (which can pattern different geometry devices out of different epitaxial layers), and finally 4) the use of a polymer planarization and passivation process (which provides quasi-planarization in the vicinity of separately grown devices possibly of slightly different height and smooth interconnection surface between them and from their top surfaces to the substrate level).

Here, we demonstrate the use of this multigrowth integration technique for the successful implementation of an integrated photonic switch that incorporates a quantum-well electroabsorption waveguide modulator and a surface-illuminated mesa photodiode along with electrical components as a part of an on-chip integrated circuit. This integrated device exhibits efficient operation at high speeds due to its compact and low-parasitic implementation using this monolithic integration technique.

References

[1] L. A. Coldren, "Widely-tunable chip-scale transmitters and wavelength converters," *Proc. OSA Tech. Dig., Optical Society of America, Integrated Photonics Research (IPR)*, Washington, DC, pp. 6–8, 2003.

[2] J. Hutchinson, J.-F. Zheng, J. S. Barton, M. L. Masanovic, M. N. Sysak, J. A. Henness, L. A. Johansson, D. J. Blumenthal, L. A. Coldren, H. V. Demir, V. A. Sabnis, O. Fidaner, J. S. Harris Jr., and D. A. B. Miller, "Indium phosphide based wavelength conversion for high speed optical networks," *Intel Technol. J.*, vol. 8, no. 2, pp. 161–171, 2004.

[3] J. W. Raring, E. J. Skogen, L. A. Johansson, M. N. Sysak, S. P. DenBaars, and L. A. Coldren, "Widely tunable negative-chirp SG-DBR laser/EA-modulated transmitter," *J. Lightw. Technol.*, vol. 23, no. 1, pp. 80–86, Jan. 2005.

[4] K. Takahata, Y. Muramoto, H. Fukano, K. Kato, A. Kozen, O. Nakajima, and Y. Matsuoka, "46.5-GHz-bandwidth monolithic receiver OEIC consisting of a waveguide *p-i-n* photodiode and a HEMT distributed amplifier," *IEEE Photon. Technol. Lett.*, vol. 10, no. 8, pp. 1150–1152, Aug. 1998.

[5] V. A. Sabnis, H. V. Demir, O. Fidaner, J. S. Harris Jr., D. A. B. Miller, J.-F. Zheng, N. Li, T.-C. Wu, H.-T. Chen, and Y.-M. Houng, "Optically-controlled electroabsorption modulators for unconstrained wavelength conversion," *Appl. Phys. Lett.*, vol. 84, no. 4, pp. 469–471, 2004.

[6] H. V. Demir, V. A. Sabnis, O. Fidaner, J.-F. Zheng, J. S. Harris Jr., and D. A. B. Miller, "Multifunctional integrated photonic switches," *IEEE Sel. Topics Quantum Electron.*, vol. 11, no. 1, pp. 86–96, Jan./Feb. 2005.

[7] V. A. Sabnis, H. V. Demir, O. Fidaner, J. S. Harris Jr., D. A. B. Miller, J.-F. Zheng, N. Li, T.-C. Wu, and Y.-M. Houng, "Optically-switched dual-diode electroabsorption modulators," in *Proc. OSA Conf. Integrated Photonics Research (IPR), OSA Tech. Dig. Opt. Soc. of America*, Paper IMB3, Washington, DC, 2003, pp. 12–14.

[8] H. V. Demir, J.-F. Zheng, V. A. Sabnis, O. Fidaner, J. P. Hanberg, J. S. Harris, Jr., and D. A. B. Miller, "Self-aligning planarization and passivation in the integration of III–V semiconductor devices," *IEEE Trans. Semicond. Manuf.*, vol. 18, no. 1, pp. 182–189, Feb. 2005.

[9] J.-F. Zheng, J. P. Hanberg, H. V. Demir, V. A. Sabnis, O. Fidaner, J. S. Harris Jr., and D. A. B. Miller, "Novel passivation and planarization in the integration of III–V semiconductor devices," in *Proc. SPIE Photonics West Conference*, Paper 5356-9, San Jose, CA, Jan. 24–29, 2004.

[10] H. Yasaka, M. Okuno, and H. Sugahara, "Device technologies for photonic networks," *NTT Tech. Rev.*, vol. 1, no. 8, pp. 49–59, 2003.

[11] S. Kodama, T. Ito, N. Watanabe, S. Kondo, H. Takeuchi, H. Ito, and T. Ishibashi, "200 Gbit/s monolithic photodiode-electroabsorption modulator optical gate," in *Proc. Device Research Conf. (DRC)*, Notre Dame, IN, 2001, pp. 151–52.

[12] H. Kitabayashi, Y. Umeda, T. Furuta, N. Watanabe, T. Akeyoshi, Y. Yamane, K. Murata, N. Shimizu, and Y. Ishii, "Monolithic integration technology using InP-based HEMT's and a uni-traveling-carrier-photodiode for over 40 Gb/s digital OEIC," in *Proc. Int. Conf. Indium Phosphide Related Materials*, Williamsburg, VA, USA, 2000, pp. 329–332.

[13] U. Eriksson, P. Evaldsson, and K. Streubel, "Fabrication of a 1.55-μm VCSEL and an InGaAsP-InP HBT from a common epitaxial structure," *IEEE Photon. Technol. Lett.*, vol. 11, no. 4, pp. 403–405, Apr. 1999.

[14] H. V. Demir, V. A. Sabnis, O. Fidaner, J. S. Harris, Jr., D. A. B. Miller, and J.-F. Zheng, "Dual-diode quantum-well modulator for C-band wavelength conversion and broadcasting," *OSA Opt. Express*, vol. 12, no. 2, pp. 310–316, 2004.

[15] D. A. B. Miller, D. S. Chemla, T. C. Damen, A. C. Gossard, W. Wiegmann, T. H. Wood, and C. A. Burrus, "Bandedge electro-absorption in quantum well structures: The quantum confined Stark effect," *Phys. Rev. Lett.*, vol. 53, pp. 2173–2177, 1984.

[16] H. V. Demir, V. A. Sabnis, J.-F. Zheng, O. Fidaner, J. S. Harris, Jr., and D. A. B. Miller, "Scalable wavelength-converting crossbar switches," *IEEE Photon. Technol. Lett.*, vol. 16, no. 10, pp. 2305–2307, Oct. 2004.

[17] O. Fidaner, H. V. Demir, V. A. Sabnis, J. S. Harris, Jr., D. A. B. Miller, and J.-F. Zheng, "Electrically-reconfigurable multifunctional integrated phonic switches," in *Proc. 17th Annu. Meeting IEEE LEOS*, Rio Grande, Puerto Rico, vol. 2, Nov. 2004, pp. 455–456.

[18] V. A. Sabnis, H. V. Demir, M. B. Yairi, J. S. Harris, Jr., and D. A. B. Miller, "High-speed, optical switching based on diffusive conduction in an optical waveguide with surface-normal optical control," *J. Appl. Phys.*, vol. 95, no. 5, pp. 2258–2263, 2004.

[19] T. Van Caenegem, I. Moerman, and P. Demeester, "Selective area growth on planar masked InP substrates by metal organic vapour phase epitaxy (MOVPE)," *Progr. Cryst. Growth Characterization*, vol. 35, no. 2–4, pp. 263–288, 1997.

[20] M. Ida, N. Shigekawa, T. Furuta, H. Ito, and T. Kobayashi, "Compositional change near the mask edge in selective InGaAs growth by low temperature MOCVD," *J. Cryst. Growth*, vol. 158, pp. 437–442, 1996.

[21] L. Silvestre, A. Ougazzaden, D. Delprat, A. Ramdane, C. Daguet, and G. Patriarche, "Study of growth rate and composition variations in metalorganic vapour phase selective area epitaxy at atmospheric pressure and application to the growth of strained layer DBR lasers," *J. Cryst. Growth*, vol. 170, pp. 639–644, 1997.

[22] T. Itagaki, M. Takemi, T. Takiguchi, T. Kimura, Y. Mihashi, and S. Takamiya, "Effects of the mask geometry on the selective-area growth by metalorganic chemical vapor deposition," in *Proc. 22nd Int. Symp. Compound Semiconductors*, 1995, pp. 127–132.

[23] G. B. Stringfellow, *Organometallic Vapor-Phase Epitaxy*. New York: Academic, 1989.

[24] A. R. Clawson, "Guide to references on III–V semiconductor chemical etching," *Mater. Sci. Eng. R-Rep.*, vol. 31, pp. 1–438, 2001.

[25] J. Schramm, "Reactive Ion Etching of Indium-Based Compounds Using Methane-Hydrogen-Argon," Ph.D. dissertation, Univ. Calif., Santa Barbara, 1995.

[26] M. L. Lovejoy, G. A. Patrizi, D. J. Rieger, and J. C. Barbour, "Thin-film tantalum-nitride resistor technology for phosphide-based optoelectronics," *Thin Solid Films*, vol. 290–291, pp. 513–517, 1996.

Vijit A. Sabnis (S'96–M'04) received the B.S. degree (highest honors, honors program) in electrical engineering and computer sciences from the University of California, Berkeley, in 1995. He received the M.S. and Ph.D. degrees in electrical engineering from Stanford University, Stanford, CA, in 1997 and 2003, respectively. At Stanford University, he studied under Professors James S. Harris, Jr., and David A. B. Miller. His doctoral research was in the areas of epitaxial growth, fabrication, simulation, and characterization of optically controlled electroabsorption modulators.

Since 2003, he has been employed at Translucent Incorporated, Palo Alto, CA, where he is investigating new materials for electronic and photonic applications. He has published over 15 journal and conference papers and holds three patents.

Dr. Sabnis is a Member of the Optical Society of America. He received the National Science Foundation Graduate Fellowship from 1996 to 1999.

Hilmi Volkan Demir (S'98–M'04) received the B.Sc. degree in electrical and electronics engineering from Bilkent University, Ankara, Turkey, in 1998. He received the M.S. and Ph.D. degrees in electrical engineering from Stanford University, Stanford, CA, in 2000 and 2004, respectively. At Stanford University, his doctoral research under Professors David A. B. Miller and James S. Harris, Jr., focused on invention, design, fabrication, testing, and modeling of multifunctional integrated photonic switches; his Ph.D. dissertation led to the world's first wavelength-converting crossbar switches.

In September 2004, he joined Bilkent University, where he is currently Assistant Professor of Physics. He is also Associate Director of Bilkent Nanotechnology Research Center and a Faculty Member of Bilkent Advanced Research Laboratory. He has published more than 20 journal and conference papers, presented more than ten invited talks, co-translated two books, and disclosed four U.S. patents (two granted, one filed, one in continuation).

Dr. Demir is a recipient of the Stanford Intel Research Assistantship (2000–2004), the Edward L. Ginzton Fellowship (1998–1999), and the Bilkent Board of Trustees Scholarship (1994–1998). He was one of the Stanford–Berkeley Innovator's Challenge Finalists, in 2003, and an invited participant of London International Youth Science Forum, London, U.K., in 1994.

Onur Fidaner (S'00) received the B.Sc. degree in electrical and electronics engineering from Middle East Technical University (METU), Ankara, Turkey, in 2001 and the M.S. degree in electrical engineering from Stanford University, Stanford, CA, in 2003. He is a Lucent Technologies Stanford Graduate Fellowship Student at Stanford University and he is currently working toward the Ph.D. degree in electrical engineering under Prof. David A. B. Miller.

His research involves investigating new integrated multifunctional photonic devices with quantum well structures on both III–V semiconductors and silicon.

Jun-Fei Zheng received the Ph.D. degree in materials science from University of California, Berkeley, in 1994.

Since then, he has been with Intel Corporation working on silicon process technology development, advanced MOS transistors, and photonic and optoelectronic devices. He was with Intel Strategic Technology Group and an Intel Researcher-in-Residence at Stanford University from 2001 to 2004. Currently, he is a Senior Staff Scientist at Intel Strategic Technology Group and an Intel Visiting Fellow at Yale University, New Haven, CT.

James S. Harris (F'88) received the B.S., M.S., and Ph.D. degrees in electrical engineering from Stanford University, Stanford, CA, in 1964, 1965, and 1969, respectively.

He is the James and Ellenor Chesebrough Professor of Engineering at Stanford University. In 1969, he joined the Rockwell International Science Center, Thousand Oaks, CA, where he was one of the key contributors in developing their preeminent position in GaAs device technology. In 1982, he joined the Solid State Electronics Laboratory, Stanford University, as Professor of Electrical Engineering. He served as the Director of the Solid State Electronics Laboratory at Stanford University from 1981 to 1988. His current research interests are in the physics and application of ultrasmall structures to new electronic and optoelectronic devices and high-speed integrated circuits and MBE growth coupled with a scanning-probed-induced oxidation for fabrication of nano three-dimensional structures. He has more than 500 publications in these areas.

Dr. Harris, Jr., is a Fellow of the American Physical Society and he received the Heinrich Walker Medal, IEEE Third Millenium Medal, and the 2000 IEEE Morris N. Liebmann Memorial Award for his contributions to GaAs devices and technology.

David A. B. Miller (M'84–SM'89–F'95) received the B.Sc. degree from St. Andrews University, St. Andrews, U.K., and the Ph.D. degree from Heriot-Watt University, Edinburgh, U.K., in 1979.

From 1981 to 1996, he was with Bell Laboratories, and from 1987, as a department head, formerly of the Advanced Photonics Research Department. Currently, he is the W. M. Keck Professor of Electrical Engineering at Stanford University, Stanford, CA, and the Director of the Ginzton and Solid State and Photonics Laboratories, Stanford, CA. His research interests include quantum-well optoelectronic and nanophotonic physics and devices, and fundamental and applications of optics in information, sensing, switching, and processing. He has published more than 200 scientific papers, and holds over 55 patents.

Dr. Miller has served as a Board member for both the Optical Society of America (OSA) and IEEE Lasers and Electro-Optics Society (LEOS), and in various other society and conference committees. He was President of the IEEE Lasers and Electro-Optics Society in 1995. He was awarded the Adolph Lomb Medal and the R. W. Wood Prize from the OSA, the International Prize in Optics from the International Commission for Optics, and the IEEE Third Millennium Medal. He is a Fellow of the Royal Societies of London and Edinburgh, OSA, and the American Physics Society (APS), and holds honorary degree from the Vrije Universiteit Brussel and Heriot-Watt University.

Nelson Li, photograph and biography not available at the time of publication.

Ta-Chung Wu, photograph and biography not available at the time of publication.

H.-T.Chen, photograph and biography not available at the time of publication.

Yu-Min Houng, photograph and biography not available at the time of publication.